applied sciences

MDPI

Article

Calibration of Acoustic Emission Parameters in Relation to the Equilibrium Moisture Content Variations in a *Pinus sylvestris* Beam

Beatrice Bartolucci [1], Francesca Frasca [1], Anna Maria Siani [1] and Chiara Bertolin [2,*]

[1] Department of Physics, Sapienza University of Rome, Piazzale Aldo Moro 5, 00185 Rome, Italy; bartolucci.1710376@studenti.uniroma1.it (B.B.); f.frasca@uniroma1.it (F.F.); annamaria.siani@uniroma1.it (A.M.S.)

[2] Department of Mechanical and Industrial Engineering, Norwegian University of Science and Technology, Richard Birkelands vei 2B, Gløshaugen, 7491 Trondheim, Norway

* Correspondence: chiara.bertolin@ntnu.no

Abstract: Under constant temperature conditions, air relative humidity variations affect hygroscopic objects, such as wood, modifying their moisture content and provoking, at low values, damages and fractures. The parameters (amplitude, counts, and energy) derived from the acoustic emission non-destructive technique are calibrated with respect to equilibrium moisture content values using 14 samplings of *Pinus sylvestris*. The experimental procedure uses multi-technique approaches involving a universal testing machine, digital image correlation, and acoustic emissions, and notes that the three parameters of acoustic emission strictly depend on the equilibrium moisture content. For a better interpretation, a statistical approach is applied to model the equilibrium moisture content variations radially and longitudinally. Amplitude, counts, and energy are calibrated as a function of the equilibrium moisture content, indicating that all three parameters are necessary to have an integral vision of the conservation of a wooden material. Moreover, the shape of the macro-fractures that occur at the surface can be associated with the level of moisture or dryness of the sample. Finally, the proposed method can be used in situ because, through acoustic emission monitoring, it is possible to quantify the fingerprint of the state of conservation of a material.

Keywords: wood; acoustic emission; non-destructive evaluation; equilibrium moisture content; cultural heritage; condition monitoring; fracture behavior; material evaluation

Citation: Bartolucci, B.; Frasca, F.; Siani, A.M.; Bertolin, C. Calibration of Acoustic Emission Parameters in Relation to the Equilibrium Moisture Content Variations in a *Pinus sylvestris* Beam. *Appl. Sci.* **2021**, *11*, 5236. https://doi.org/10.3390/app11115236

Academic Editor: Giuseppe Lacidogna

Received: 10 May 2021
Accepted: 2 June 2021
Published: 4 June 2021

1. Introduction

Wood has been one of the most widely used hygroscopic materials since ancient times, both for buildings and works of art, due to its strength and hardness properties. Resistance and elasticity are strictly related to the shape and chemical composition of the plant cell walls, making wood's tensile strength value (850 kg/cm^2) the highest after those of steel and cast iron [1].

Wood tends to be at thermodynamic equilibrium with surrounding environmental conditions by absorbing and desorbing moisture. These processes can cause mechanical degradation due to the swelling and shrinkage of fibers and can also lead to the formation of cracks. Since wood is an orthotropic material, the main anatomical directions of wood—longitudinal, radial, and tangential—are characterized by different water diffusion coefficients [2].

Wood is the main material studied in the framework of the international project "SyMBoL—Sustainable Management of heritage Buildings in a Long-term perspective" (2018–2021) [3]. The SyMBoL project focused on searching for adequate environmental conditions for the conservation of collections and the interiors of the most significant Norwegian historic wooden buildings, the Medieval *Stave Churches*, which can potentially be affected by climate change, mass tourism, and internal heating issues [4]. The SyMBoL

project focused on a better understanding of the amplitude and duration of indoor climate change, which may induce mechanical decay in the wood and polychromes of these preserved churches. In the SyMBoL framework, the study of the mechanical properties of pine wood, i.e., Scots pine (*Pinus sylvestris* L.), is mainly performed by means of the acoustic emission non-destructive technique. Pine is a softwood with a density ranging between 365 kg/m^3 and 590 kg/m^3. Specifically, Scots pine shows a density that ranges between 505 kg/m^3 and 540 kg/m^3 when the moisture content is varied between 12% and 12.4% [5]. Indeed, recently, Li et al. demonstrated that moisture content has a direct effect on the mechanical properties of wood by modifying orthotropic viscoelastic performance during a water loss process [6], and other recent studies assessed that this change in the mechanical behaviour of wood leads to differences in energy release for acoustic emission monitoring during fracture when moisture content changes [7,8]. Indeed, fluctuations in ambient relative humidity (RH) are considered the main factor that contributes to the deterioration of wooden objects and acoustic emissions are able to detect the stress induced by such climate variability [9]. Acoustic emissions are the energy released by a structure that is undergoing deformation due to micro and macro fractures. The energy propagates through the material as ultrasound and sound waves, and can be detected at the surface using piezoelectric transducers (AE sensors), which convert the surface vibrations into an electrical signal [10]. The acoustic waves propagate inside wooden material in different ways according to the type of wood [11] or the directionality of wood (radial, tangential, or longitudinal) within the same wood species [10]. Therefore, the acoustic emission monitoring has a wide variety of applications: it is an early warning technique that is useful for preventive detection of the stability of a structure before it can suffer damage from earthquakes or landslides [12]; it can be useful to detect the type and direction of grains in a wood [13]; and it can estimate moisture content in wooden objects [14,15] pinpointing its response to environmental variability [10,16].

For the above reasons, the combined use of acoustic emission (AE) and digital image correlation (DIC), both non-destructive techniques (NDTs), were set up in a laboratory to detect the occurrence and progression of fractures of wooden samples at different moisture content conditions during tensile tests, performed using a universal testing machine (UTM). The tested samples were cut from a naturally dried Scots pine beam.

The tensile tests enabled the study of the relationship between acoustic emission outputs (amplitude, counts, and energy) and the moisture content in Scots pine samples. Indeed, this laboratory test can be preparatory to apply the AE technique in situ and to calibrate it against moisture-induced stress on massive pine beams.

The paper is structured in three sections: Section 2 (Materials and Methods) provides a description of the experimental setup and laboratory tests on the wood samples. The Results section describes the outcomes of the experimental research based on acoustic emissions and their relationships with the equilibrium moisture content. Evaluations of the results are provided in the Conclusions.

2. Materials and Methods

The methodology, schematized in Figure 1, was applied to 14 Scots pine "simil-CT" (compact tension) samples, cut according to schema in Figure 1a, and tested using a three-technique experimental setup (Figure 1b).

The experimental setup was based on tensile tests carried out by means of a universal testing machine (UTM) with the aim of producing a fracture in the radial–tangential plane (RT), i.e., perpendicular to the grain of the beam, as it is much more sensible in terms of the capacity load of building components made from softwood species [17]. In addition, the fracture progression was constantly monitored using a digital image correlation (DIC) camera and two acoustic emission sensors.

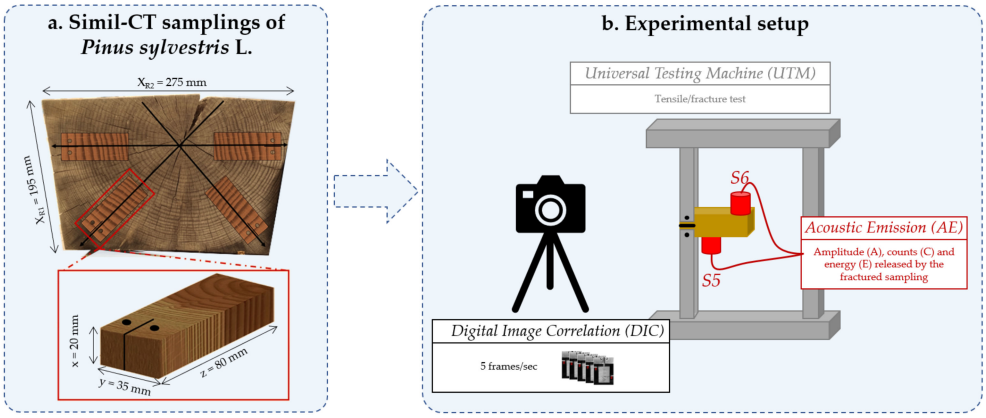

Figure 1. (**a**) Simil-CT samples cut from Scots pine (*Pinus sylvestris* L.) beam, naturally dried out. (**b**) Experimental setup: universal testing machine (UTM) for tensile fracture tests, digital image correlation (DIC) for evaluating the elongation of the fracture, and two sensors, indicated by code S5 and S6, for the acoustic emissions (AE) to detect amplitude (A), counts (C), and energy (E) released by the fracture.

After a long-term drying process, the detection of AE parameters emitted by samples at different stages of drying completeness allowed to examine the influence of moisture content on the state of conservation of wooden slices in the beam as well as their capability to release elastic energy.

2.1. Experimental Setup

Tensile tests were performed using a UTM (MTS—Measure Test Simulate® [18]), by applying a displacement rate of 0.5 mm/min. During each tensile test, two types of fracture progressions were distinguished: brittle-like and ductile-like fracture progressions [16]. They differ in the rate of deformation of a material—the former being elastic and fast, the latter being plastic and slow—as well as in terms of the type of released energy.

A DIC Stingray_F-504 camera taking 5 frames/s, was used to visually detect the progression of fracture and monitor it over time, allowing to measure its length in millimeters [19].

AE allowed to detect the energy released by the fracture. In this study, two sensors (frequency operating range = 100–900 kHz), manufactured by Vallen Systeme [20], were used: sensor S5 was placed closer to the 20 mm pre-crack and sensor S6 was positioned farther from the pre-crack (Figure 1b). The position of the AE sensors was chosen taking both the geometrical constraint of samples and the necessity to avoid spurious signals due to clamps into account. In this way, S6 was not affected by the background noise of the UTM, whereas S5 on the other hand was allowed to have a signal backup. The AE technique provided the following three parameters:

- Amplitude (A): is the peak in decibel during an acoustic emission event; it shows the disturbance level and the response of the sensor after power/energy loss. The set threshold value was 40 dB.
- Counts (C): it shows the number of times a signal exceeds a set threshold value. Real events have high counts.
- Energy (E): is the elastic energy released during an acoustic emission event, measured in arbitrary units (or energy units, e.u. = $10^{-14}V^2s$). The AE energy can be determined using Equation (1), integrating the absolute or the squared values of the signal's voltage curve over time [21]. Real events have high energy units.

$$E = \int_{t_0}^{t} U^2(t)dt \quad (1)$$

Raw data collected through the experimental setup were organized in order to determine the synchronicity between the fracture event (UTM), its elongation (DIC) and the associated AE signals. The analysis was focused on brittle fractures, because under these circumstances, the energy released by the material and detected by the AE is mainly elastic.

2.2. Scots Pine Beam and Its Thermodinamic Equilibrium

2.2.1. Simil-CT Samplings of Scots Pine

A large Scots pine beam (*Pinus sylvestris* L.) (Figure 2) was used in this study: X_{R1} = 195 mm, X_{R2} = 275 mm, X_L = 968 mm. X_{R1} and X_{R2} are the radial dimensions of the beam, X_L is the longitudinal direction; hereafter X_{R1} will be simply named as X_R. Progressing through the pith—along the longitudinal section—the beam had two faces (195 mm × 275 mm) exposed to external conditions. The beam was cut along its main axis into adjacent rectangular slices with thicknesses of 20 mm, numbered from 1 to 25. Along the radial section of each slice, four faces (i.e., the lateral surface of the beam) were in direct contact with the surrounding environment. The first six slices, together with slices 18 to 22, were excluded from analyses as they showed a strong fracture pattern due to the uneven change in environmental conditions, as described in the next paragraph. Consequently, the slices considered for further sample preparation were those numbered from 7 to 17 and from 23 to 25.

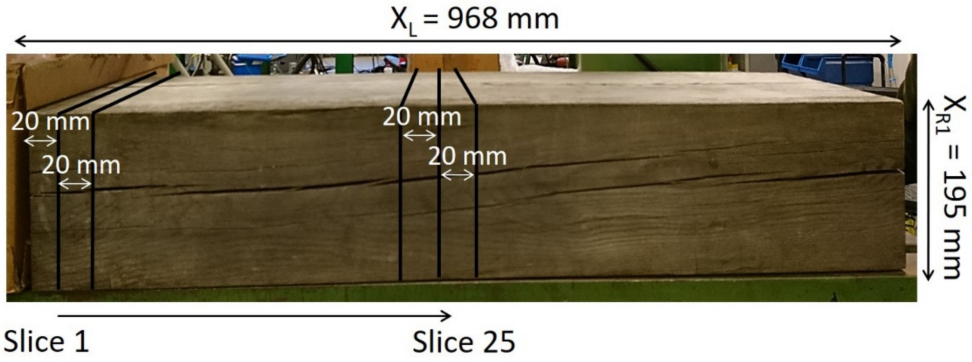

Figure 2. Rectangular parallelepiped of the *Pinus sylvestris* (Scots pine beam). The area of the beam that was cut in slices had dimensions and are indicated with uppercase letters: X_{R1} = 195 mm, X_{R2} = 275 mm, X_L = 968 mm.

Three or four "simil-CT" samples were cut from each slice with the following dimensions, indicated by lowercase letters: x = 20 mm, y = 35 mm, and z = 80 mm, as shown in Figure 1a. Each sample was associated with an ID number, coded as the letter "S" followed by the number of the slice from which it originated and the count of the produced sampling; for example, S072 is the second sample cut off from slice 7. Figure 1a shows the way in which the samples were cut from the beam, avoiding the major shrinkage defects. The samples were cut in the radial–tangential direction, known as the RT plane. Two gap holes were carved in each sample close to the external side of the beam to tightly clamp the sample to the UTM during the tensile tests. Between the two holes, a 20 mm pre-crack was also carved.

Tensile tests for failure analysis were carried out on all samples. The 50th and 90th percentiles of the angle of fracture of each sample, with respect to the grain direction, were calculated. It was observed that, when the 50th percentile of the angle was >9°, there were internal defects that caused the samples to break following the curvature of the ring. The wooden beam can be defined as quasi-parallel-to-grain, with some internal defects, such as local waving of the grain and/or knots. For this reason, these samples were not considered for further analysis. The remaining 14 samplings were linked to the areas of origin from each slice in the beam with comparable provenances in term of the progression of rings, from the pith to the external surface. Two groups were identified: Group 1 and Group 2 were, respectively, associated with samples cut parallel to the grain and not parallel to the

grain from the slices. This identification was obtained after a pixel-by-pixel analysis, which allowed understanding the directionality of each specimen based on the unique sequence of wooden rings. Table 1 shows the ID numbers of the samples with their corresponding group, their own directionality, and the 50th and 90th percentiles of the grain angle.

Table 1. ID number of the samplings, their classification into the group (1 or 2) based on the directionality in the beam slices.

ID Number	Group	Directionality	Grain Angle	
			50th percentile	90th percentile
S081, S091, S101, S111, S123, S142, S153, S173	Group 1	Parallel to grain	4°	9°
S093, S122, S143, S152, S163, S172	Group 2	Not parallel to grain	5°	10°

It is worth noticing that the percentile values of grain angles may vary depending on the carving: Figure 3 shows possible positions of samples with respect to the grain: Figure 3a shows the samples when they were carved from a slice with an angle of 0°; Figure 3b shows the samples when carved using an angle different from 0° with respect to the grain.

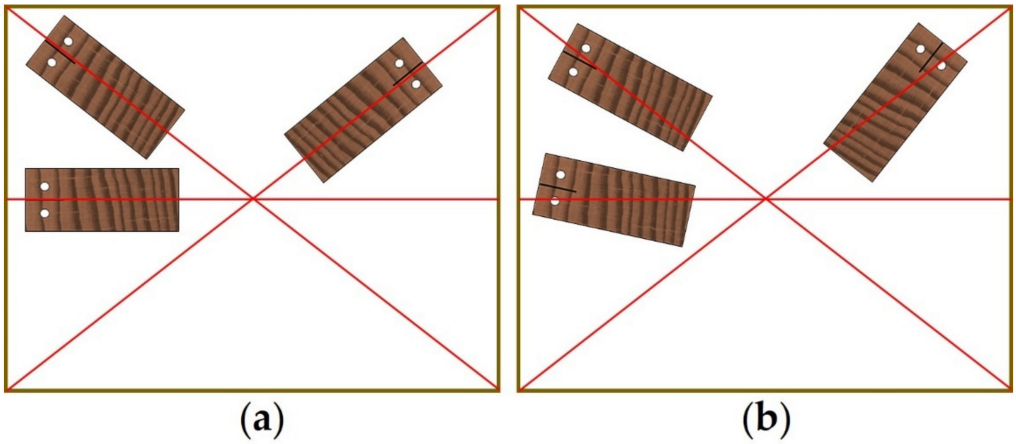

Figure 3. (**a**) Samples carved from the slice with a grain angle of 0°, i.e., fracture follows the direction of the growth rings; (**b**) samples carved with a grain angle different from 0° with respect to the growth ring direction.

2.2.2. Thermo-Dynamic Equilibrium of Moisture Content

In this study, the equilibrium moisture content (EMC) was used as the moisture gradient parameter since it only depends on the environmental conditions surrounding the beam and it is not experimental derived. The EMC was determined by calculation in each slice along the longitudinal and radial directions, because generally wood has an increase in EMC from the edge of the beam to the pith [22].

The tested Scots pine beam was left outdoors for more than two years (January 2016–August 2018) at the campus of the Norwegian University of Science and Technology (NTNU, Trondheim, Norway) [23], where there was an average temperature (T) of 5 °C and relative humidity (RH) of 85%. In September 2018, the beam was moved inside the Fatigue, Fracture and Mechanical Characterization Laboratory (NTNU campus), under new conditions of T = 21 °C and RH = 30%. It was assumed that, from 1 September 2018 until 9 February 2019 (i.e., 160 days), the beam—from its external surface to a certain depth towards the pith—reached an hygrothermal equilibrium state with the indoor conditions, the so-called equilibrium moisture content (EMC), which is expressed as the percentage of the mass of water per unit mass of anhydrous material [24]. The response of the beam to the variations in the indoor climate occurred differently along longitudinal and radial

directions, determining peculiar moisture gradients inside the wood. Since the beam was naturally dried, it was assumed that, after 160 days, only the outermost layers were in complete equilibrium with the indoor climate conditions, while the innermost layers (i.e., closer to the pith and in the middle of the beam along the longitudinal direction) were still—in some part—in equilibrium with the previously experienced outdoor climate conditions. In this way, it was possible to determine the EMC at each point of the beam using $RH_{response}$. Indeed, at a constant temperature, T (=21 °C), $RH_{response}$ is the response of a wooden material at a certain depth of the specimen with respect to adjacent material layers and environmental relative humidity. This parameter is determined using Equation (2) in [25].

$$RH_{response,i} = \frac{RH_{response,\ i-1} + \frac{RH_i}{n/3}}{1+\frac{1}{n/3}} \quad (2)$$

where RH is the relative humidity (%); $RH_{response}$ is the material response in RH (%); n is the number of data points over the response time expressed in days and multiplied by 24 h; and i is the ith day, and therefore it refers to the time expressed in days occurred since the environmental change (from day 1 to 160). Thus, RH_i was set equal to 85% in the first few days of drying (i.e., corresponding to the averaged outdoor conditions) up to 30% going towards the 160th day (i.e., approx. equal to the stable laboratory room conditions). $RH_{response}$ depends on the response time, defined as the time needed for an object to reach 95% of the end value of a step change in RH [24]. The response time depends on the geometry and the depth of the object. In this work, the $RH_{response}$ was evaluated along the radial and longitudinal axes, and was plotted in graphs showing the trend of the two anatomical directions during the period of 160 days, from 1 September 2018 to 9 February 2019.

Once obtained, the $RH_{response}$ of each slice along the longitudinal and radial directions was transformed into equilibrium moisture content, according to Equation (3), assuming a constant room temperature (21 °C) [26]. Equation (3) shows the EMC in relation to RH (and T). In this work RH is assumed as $RH_{response}$.

$$EMC = 5.9 \cdot RH\ -\ 4.7 \quad (3)$$

In the above equation, the coefficients may vary with respect to temperature and wood species [27].

In accordance with the relative humidity response provided by Equation (2), at last, after 160 days, the equilibrium moisture content (named as $EMC_{after160dd}$) is calculated with Equation (4):

$$EMC_{after\ 160dd} = \frac{EMC_i - EMC_{final}}{EMC_{initial} - EMC_{final}} \quad (4)$$

where EMC_i is the equilibrium moisture content in a point in each slice identified by the longitudinal and radial coordinates—$EMC_{initial}$ and EMC_{final}—are the equilibrium moisture contents under initial (outdoors) and final (indoors) acclimatization conditions.

2.3. Equilibrium Moisture Content Model and the Acoustic Emission Signals

EMC was evaluated along the longitudinal and the radial directions because moisture behaves differently depending on the axis or section of wood considered. For this purpose, multilinear regression was applied to analytically derive the EMC within the beam.

The radial (x_1) and longitudinal (x_2) directions were used together to understand to what extent these two independent variables affect the dependent variable of EMC (y). For this analysis, eight multiple linear regressions (Equation (5) and the equations in Appendix A) were studied:

$$y = b_0 + b_1x_1 + b_2x_2 \quad (5)$$

The adjusted coefficient of determination ($\overline{R}^2$) and the standard error (E_{STD}) were used to understand which regression model could better explain the equilibrium moisture

content gradient. Equation (5) was selected on the basis of a simple and realistic physical situation, regardless of the best statistical parameters.

In this way, at each point where a fracture elongation took place according to brittle phenomenon, the equilibrium moisture content was more specifically determined using this model.

In accordance with the procedure described in [16], the distribution of each acoustic emission parameter occurring during brittle phenomena was analyzed in order to identify the acoustic fingerprint of the species. Moreover, the cumulative sum of AE parameters was used to evaluate the sensitivity of AE with respect to dryness along the longitudinal and radial directions of the beam, and hence investigate the effect/impact of EMC changes on the mechanical properties of wood. This was a preparatory step to pinpoint how wood behaves with respect to environmental conditions and which AE parameters are more sensitive for calibration with EMC.

Finally, the energy attenuation rate along the samples at the end of the drying process (after 160 days) can be calculated as the sum of the difference between the initial and final state of EMC, from the pith to the outmost layers of the sample. Analytically, this can be expressed using Equation (6), where β is the coefficient of the energy attenuation rate.

$$\Sigma(\Delta E) = \exp(-\beta \cdot \Sigma(\Delta EMC)) \quad (6)$$

Equation (6) can be simplified by applying the Taylor series for exponential functions if ΔEMC is small, i.e., when the moisture gradient across the sampling is not appreciable. In this way, β can be defined graphically, calculating a linear best fit from the experimental datasets from Equation (7):

$$\beta = -\frac{m}{q} \quad (7)$$

where m is the angular coefficient and q is the intercept of the linear best fit.

3. Results and Discussions

3.1. Acoustic Emission Analysis

Figures 4–7 show histograms of the acoustic emission parameters. Each figure provides the number of events (NoE) registered during the test, i.e., the frequency registered during the brittle events.

Figures 4 and 5 show results of the AE parameters detected using S5 and S6, respectively, on fractured Group 1 samples, whereas Figures 6 and 7 show results for the same sensors, but on fractured Group 2 samples, respectively.

The amplitude of sensor 5 was higher than that of sensor 6. Moreover, the range between 50 and 60 dB, which was the one characterized by the greatest number of events, in the graph concerning sensor 5 was higher than that of other ranges. The differences between the ranges flattened out slightly in the case of sensor 6. The results for Group 2 were similar to those of Group 1: amplitude was characterized by events of brittle fractures in the range of 50 dB < A < 60 dB. Moreover, for both sensors, the higher count values are in the range of bin C > 30. These results are in line with those found by Bertolin et al. [16]. Concerning energy, the maximum occurrence was in the range 1000 eu < E < 5000 eu. In each graph, there are some samples which can be traced as outliers: in Group 1, samples S081 and especially S142 have higher occurrences than the average of the other samples. The same was the case for samples S143 and S172 (Group 2), which had higher values than the other samples or with respect to the average values.

Figures 8–10 show the behavior of the AE parameters with respect to the radial ($X_{R1} \approx X_R$) and the longitudinal positions (X_L) in terms of amplitude, counts, and energy for Group 1 and Group 2, respectively. The choice of using three-dimensional graphs was found to be the most adequate to define, at the same time, the dependence between the cumulative sums of amplitude, counts, and energy within the two directions of the wooden beam.

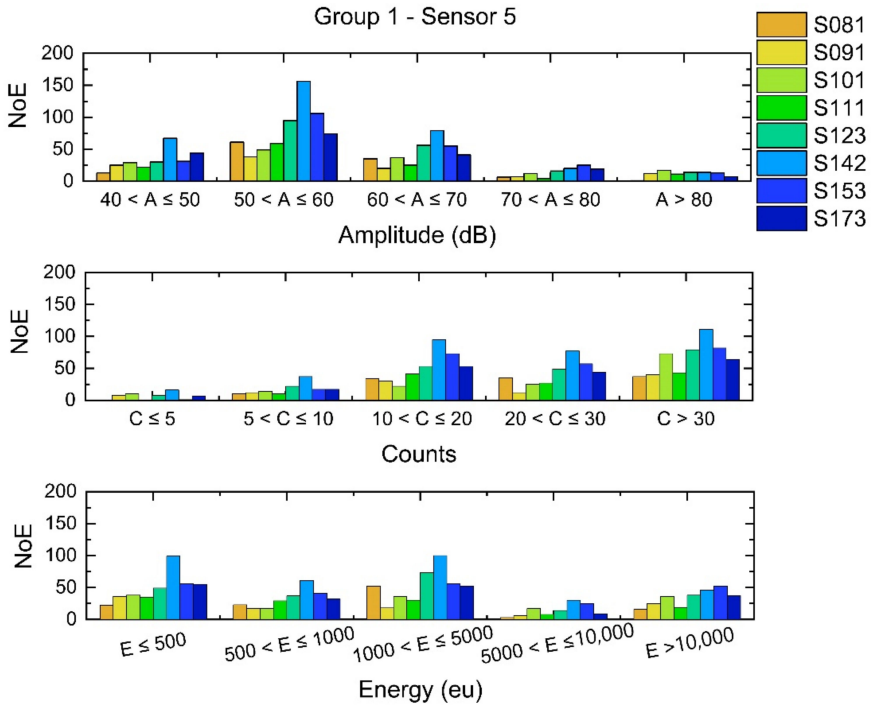

Figure 4. Number of events (NoE) registered during brittle fracture for Group 1 recorded by sensor 5. Each sample is identified by an ID number "Sxxy" corresponding to the number of slices (xx) and the count of the produced sample in the slice (y). (**Top**) amplitude; (**Middle**) counts; (**Bottom**) energy released by the fracture.

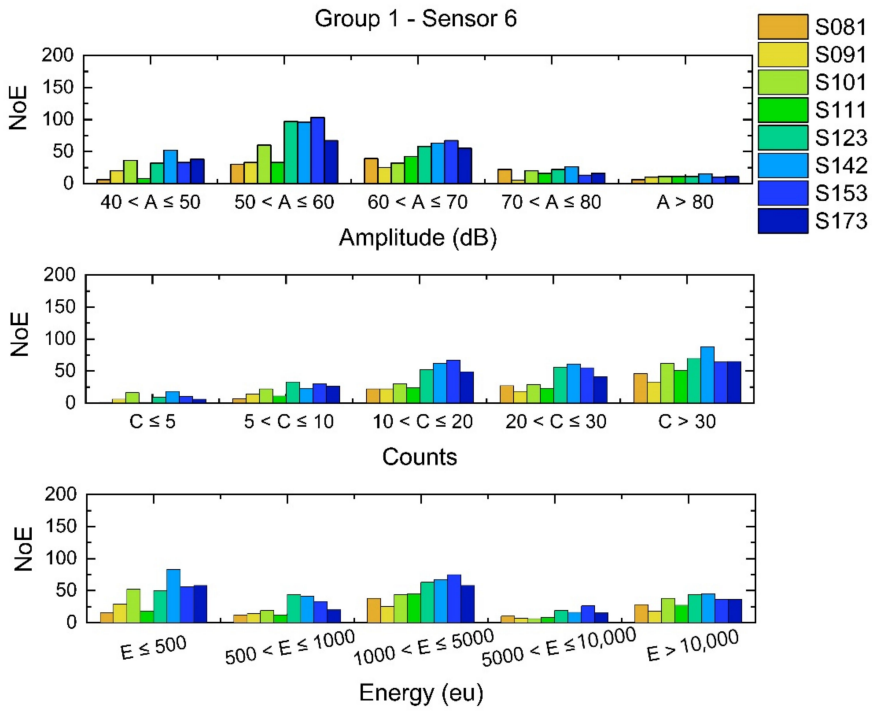

Figure 5. Number of events (NoE) registered during brittle fracture for Group 1 recorded by sensor 6. Each sample is identified by an ID number "Sxxy" corresponding to the number of slice (xx) and the count of the produced sample in the slice (y). (**Top**) amplitude; (**Middle**) counts; (**Bottom**) energy released by the fracture.

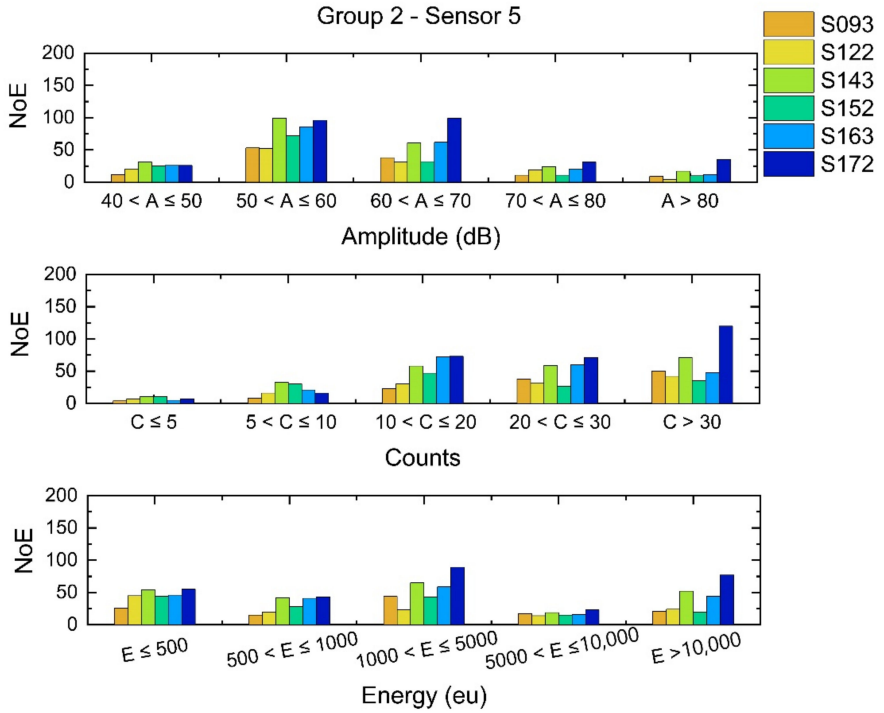

Figure 6. Number of events (NoE) registered during brittle fracture for Group 2 recorded by sensor 5. Each sample is identified by an ID number "Sxxy" corresponding to the number of slice (xx) and the count of the produced sample in the slice (y). (**Top**) amplitude; (**Middle**) counts; (**Bottom**) energy released by the fracture.

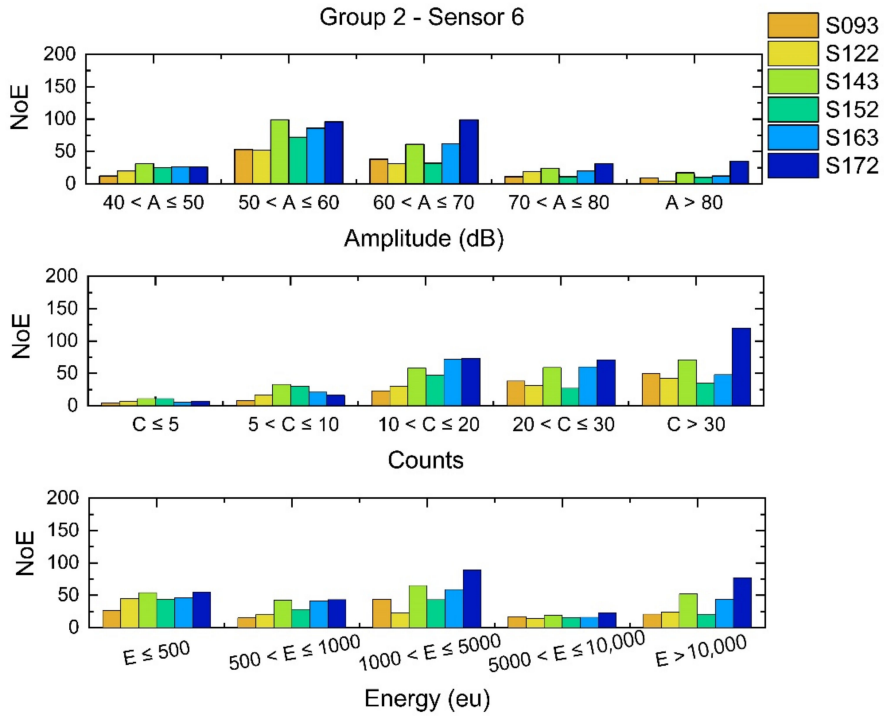

Figure 7. Number of events (NoE) registered during the brittle fracture for Group 2 recorded by sensor 6. Each sample is identified by an ID number "Sxxy" corresponding to the number of slice (xx) and the count of the produced sample in the slice (y). (**Top**) amplitude; (**Middle**) counts; (**Bottom**) energy released by the fracture.

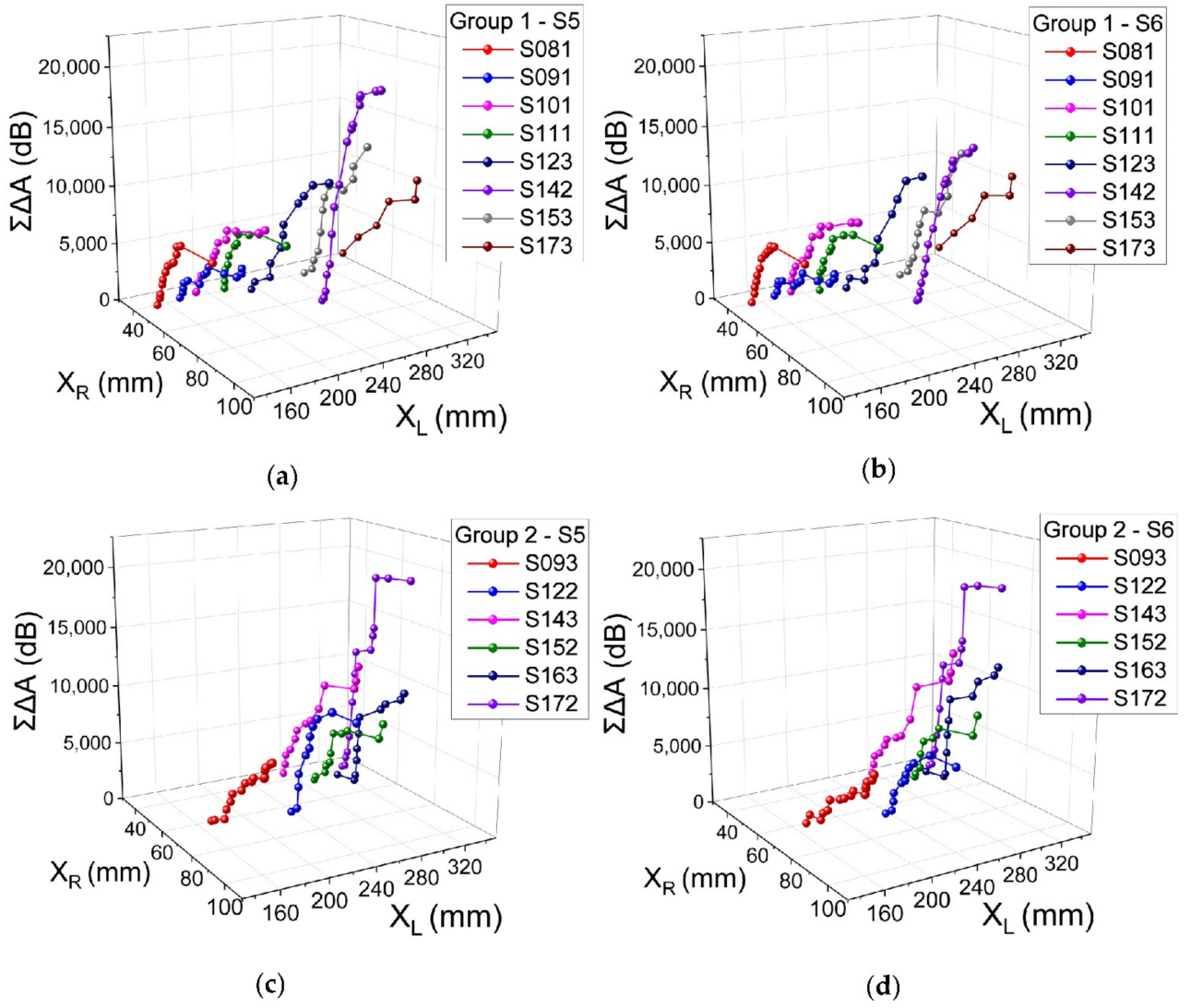

Figure 8. Three-dimensional graphs: x-axis—radial position X_R (mm); y-axis—longitudinal position X_L (mm); z-axis—cumulative sum of the amplitude, i.e., ΣΔA (dB). (**a**) Group 1, S5; (**b**) Group 1, S6; (**c**) Group 2, S5; and (**d**) Group 2, S6.

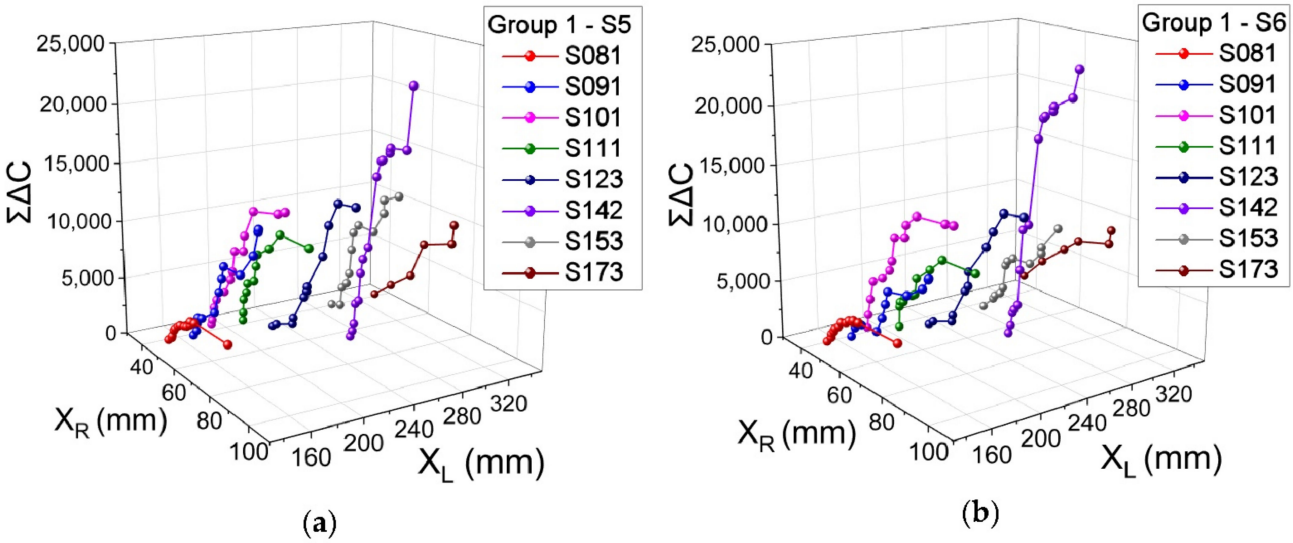

Figure 9. *Cont.*

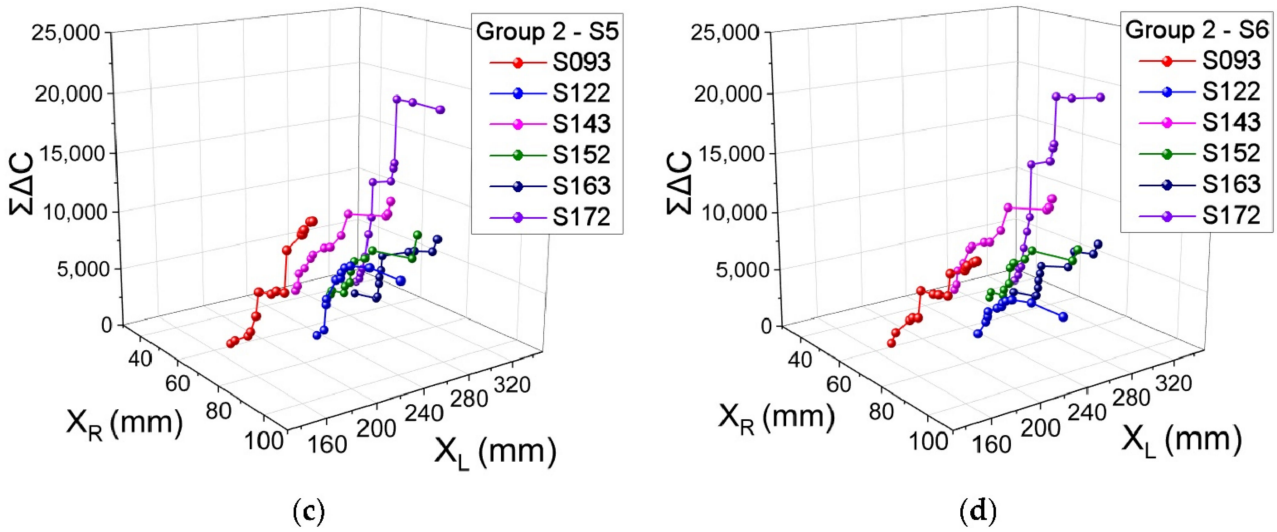

Figure 9. Three-dimensional graph: x-axis—radial position X_R (mm); y-axis—longitudinal position X_L (mm); z-axis—cumulative sum of the counts, i.e., ΣΔC. (**a**) Group 1, S5; (**b**) Group 1, S6; (**c**) Group 2, S5; and (**d**) Group 2, S6.

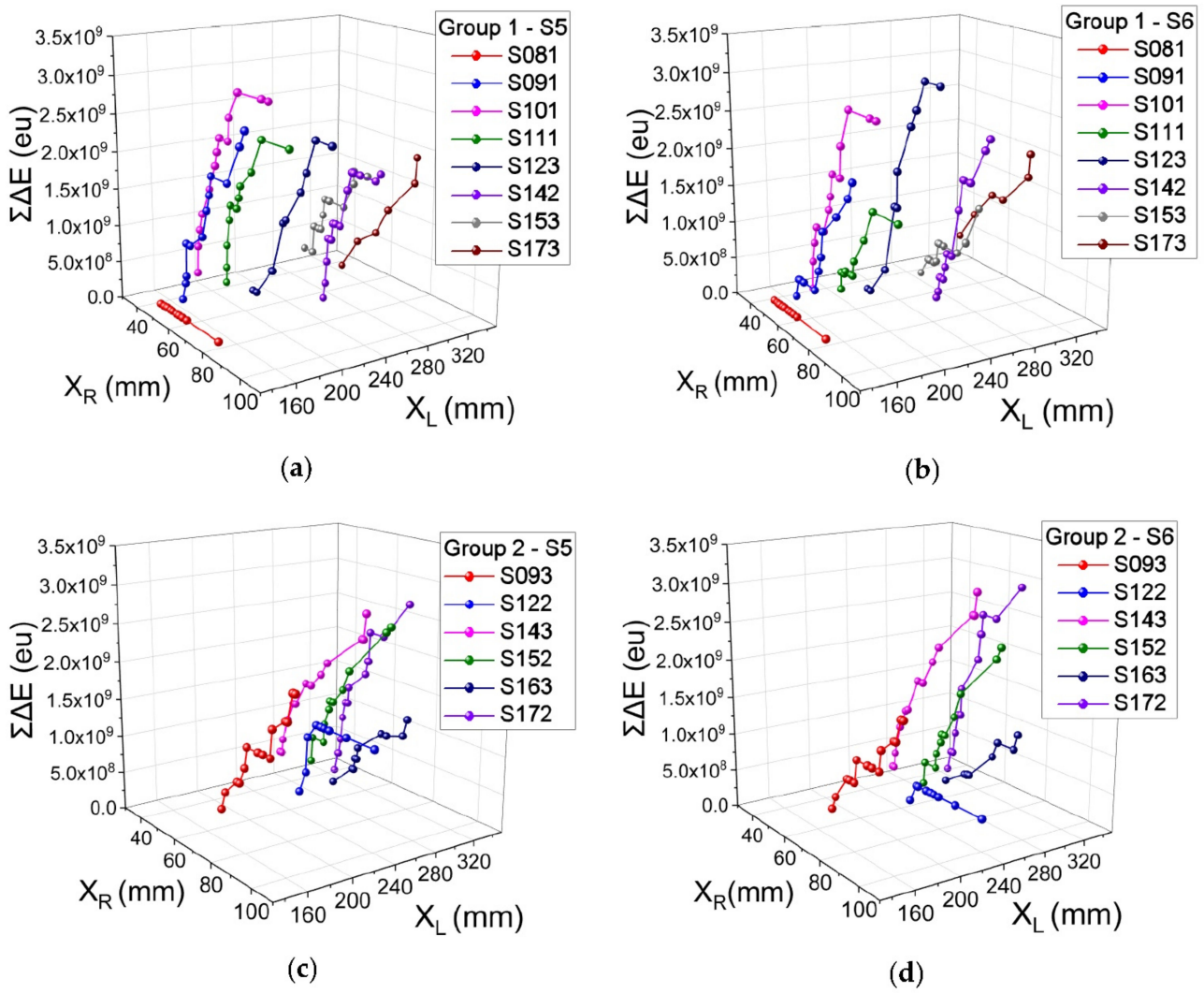

Figure 10. Three-dimensional graph: x-axis—radial position X_R (mm); y-axis—longitudinal position X_L (mm); z-axis—cumulative sum of the energy, i.e., ΣΔE (eu). (**a**) Group 1, S5; (**b**) Group 1, S6; (**c**) Group 2, S5; and (**d**) Group 2, S6.

Figure 8 (amplitude) and Figure 9 (counts) show the trends of the detected cumulative amplitude values, as a function of the radial and longitudinal positions. It was noted, as in the graphs, that the values along the longitudinal position remained constant whereas those along the radial position were more variable due to the direction of the fracture. In Figure 10, on the other hand, the energy values have a wider variability, ranging from the minimum of sampling S081 (4.72×10^6 eu) up to the maximum of sampling S101 (2.94×10^9 eu) for Group 1. Therefore, energy is a parameter that seems to depend on other factors rather than the positioning of the sample inside the wooden beam, which is representative of specific EMC values. These factors are, for example, the sensor location and the presence of defects. In the next section, the same parameters will be plotted as a function of moisture content at equilibrium, to calibrate AE with the EMC model.

All the samplings studied using 3D graphs indicate that the radial and longitudinal positioning influence the elongation of the fracture, and the radial section has more variability with respect to the longitudinal section. Consequently, both X_R and X_L can influence acoustic emission events detected during the brittle phenomenon of fracture.

3.2. Gradient of the Equilibrium Moisture Content

Since wood is an orthotropic material, moisture diffusion strongly depends on the response of the wood in the main anatomical directions to variations in surrounding environmental conditions. The analysis of $RH_{response}$ along the longitudinal direction (Figure 11a,b) highlights that only the first slices (up to a 60-mm depth) reached equilibrium with indoor environmental conditions (≈30%) within the 160 days. Figure 11c,d instead shows that, in the radial section, only the outermost layers (ca. 20 mm) were able to reach a complete balance with the laboratory environment after 160 days. In Figure 11c, the first 100 mm of layers (i.e., half of the radial size of the beam, as expressed in Figure 1a) were used in the calculation, as the moisture gradient behavior was specular.

The EMC calculations obtained using the $RH_{response}$ values trace the drying process within a single slice both in the radial and longitudinal directions. In summary, the EMCs in the first slices are in equilibrium with the surrounding air, because the $RH_{response}$ in slices 1 to 4, at the end of the 160 days, was ca 6%. Longitudinally, EMC varied from ≈6% in the outermost slices to ≈16% in the innermost slices (Figure 12a). A similar EMC anomaly with a faster rate of change is visible within the same slice (radial direction, as reported in Figure 12b), from the edge to the pith of the beam.

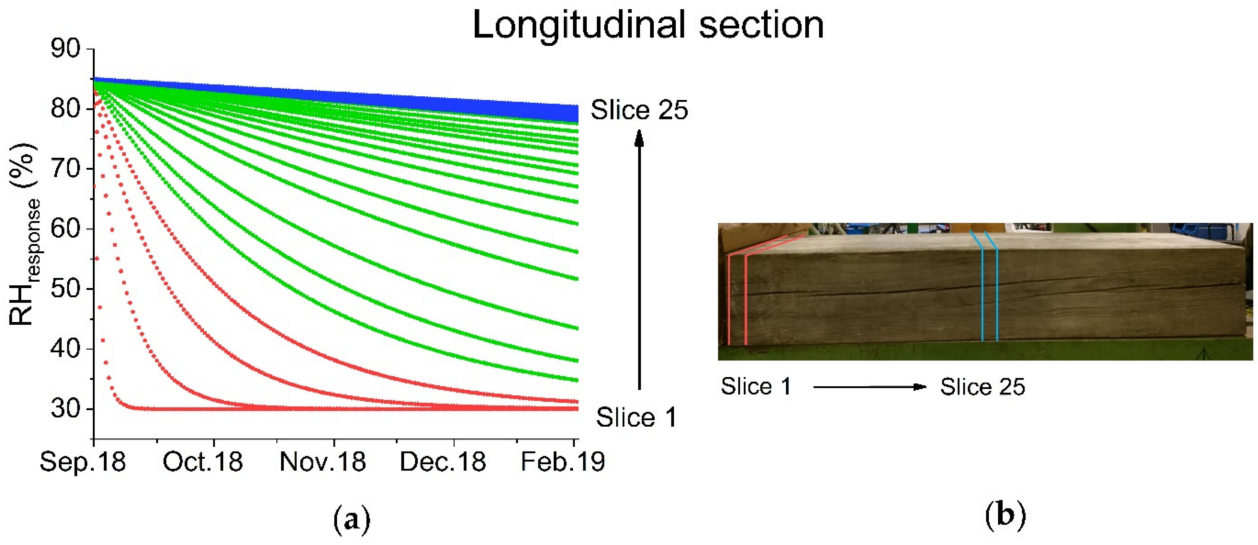

Figure 11. *Cont.*

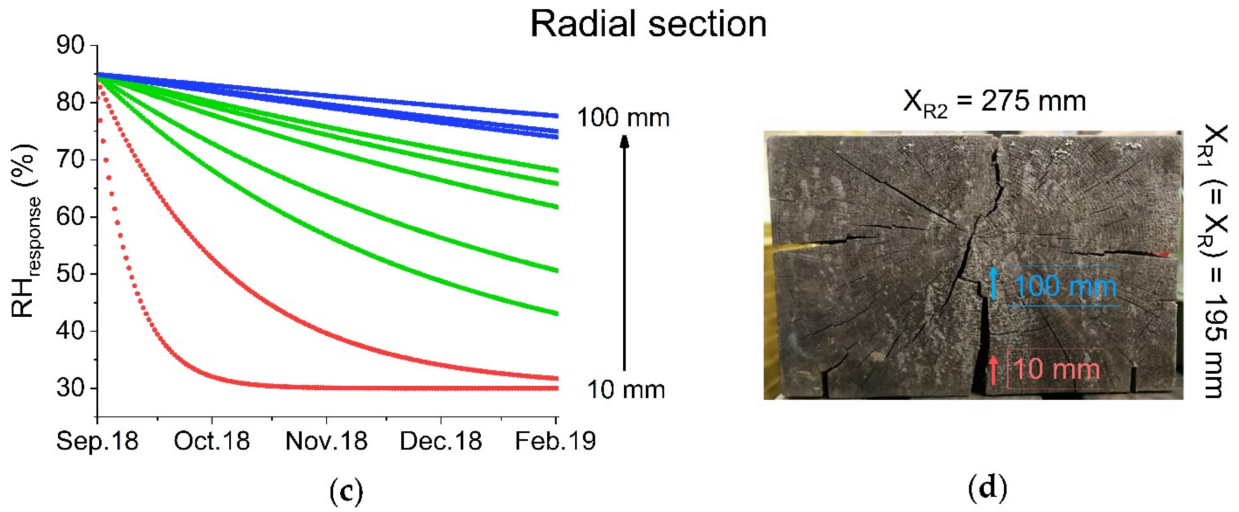

Figure 11. $RH_{response}$ (%) trend along the two main directions. (**a**) $RH_{response}$ along longitudinal direction from slice S1 (10 mm depth) to slice S25 (490 mm depth) over time. (**b**) Longitudinal axis and slices of the beam. (**c**) $RH_{response}$ along radial direction from surface (10 mm) to the pith (100 mm) of the beam over time. (**d**) Radial axis of the beam.

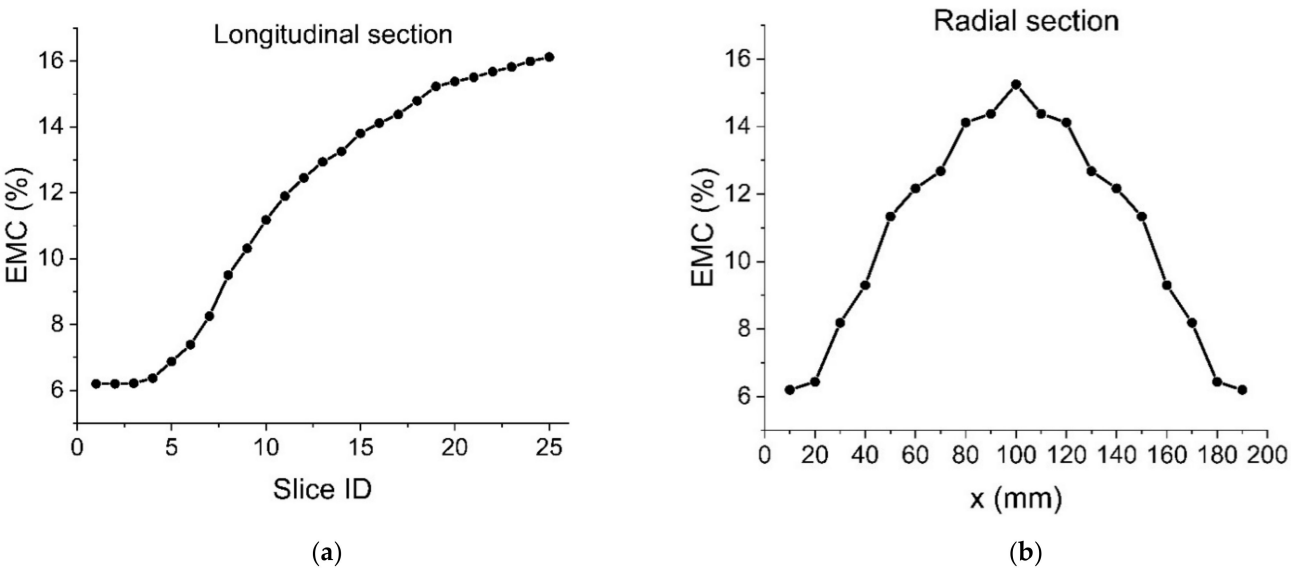

Figure 12. Final EMC values after 160 days. (**a**) EMC in longitudinal direction, as a function of the slices along the main axis of the beam (S1–10 mm; S2–30 mm; S3–50 mm … S25–490 mm). (**b**) EMC in radial direction, as a function of the radial depth within a single slice.

3.3. Acoustic Emission vs. Equilibrium Moisture Content

Figure 13 represents the EMC modelled using the regression in Equation (5), selected for the analysis.

In this graph a sub-set of data corresponding to about 6% EMC is detectable (red box), followed by data spread to a final value of 16% EMC. This behavior can be explained by the fact that the first slices respond quickly to external conditions, reaching thermodynamic equilibrium earlier than 160 days; in the central part (green box) of the graph, data are highly scattered (7% < EMC < 13%); in the final part (EMC > 13%), data are almost linearly distributed (blue box), meaning that slices were less affected by the indoor hygrothermal conditions, even after 160 days.

This model is the simplest multilinear regression that independently explains the variation of EMC in the radial and longitudinal directions, and shows a high $\overline{R}^2$ value (0.89) with a direct linear relationship with x_1 (radial direction) and x_2 (longitudinal direc-

tion). The intercept is 1.99 and the coefficients associated with x_1 and x_2 are, respectively, 8.71×10^{-2} and 1.06×10^{-2}.

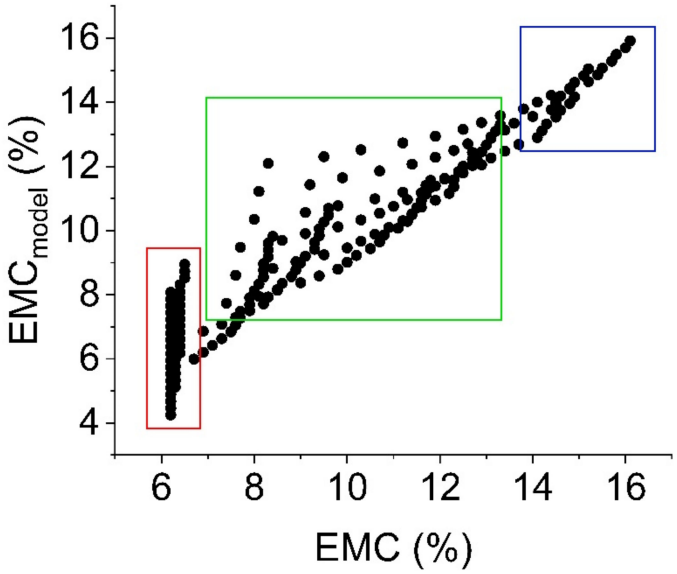

Figure 13. The selected linear multiple regression model (Equation (5)). On the abscissa, the EMC as calculated by Giordano, on the ordinate, the modelled EMC (unit %). The three boxes highlight areas that differ from each other. The red box indicates a first set of data with EMC = 6%; the green box highlights a central dataset with 7% < EMC < 13%; the blue box indicates a quasi-linear dataset with EMC > 13%.

The AE parameters of amplitude, counts, and energy can demonstrate how the wood behaves when subjected to its surrounding environment, providing information on the state of conservation, and interaction processes with the material itself until the equilibrium is achieved. Figures 14–16 show the effect of drying (ΔEMC on the x-axis) along the sample on the AE parameters recorded during fracture by both S5 and S6 for Group 1 and Group 2 (on the y-axis). ΔEMC was calculated from the initial and final EMC values after 160 days of dryness, from the pith to the outermost layers. Figure 14 illustrates the cumulative amplitude (ΣΔA, dB) emitted by samples S081, S091, S101, and S111 (Group 1), where the lower ΣΔA values (orange-colored) correspond to easily detectable events along the sample subjected to a complete drying process; otherwise, samples S123, S142, and S153 (blue-colored) show a higher cumulative amplitude in connection with events that are difficult to detect and caused by an incomplete drying process along the sample. Then, sample S173 appears to be an outlier, as it has a similar pattern of amplitude values as the first samples, described by slices 8 to 11 (S081, S091, S101, S111), although with an ΔEMC span comparable to samples S123, S142, and S153. Concerning Group 2, the same behavior of amplitude was detected by both sensors. In this case, the samples colored with the lighter colors, i.e., S093, S122, and S152, show the most reliable sensing of amplitude values. Sample S172 is the one that presents difficulties in amplitude detection because of its wet state.

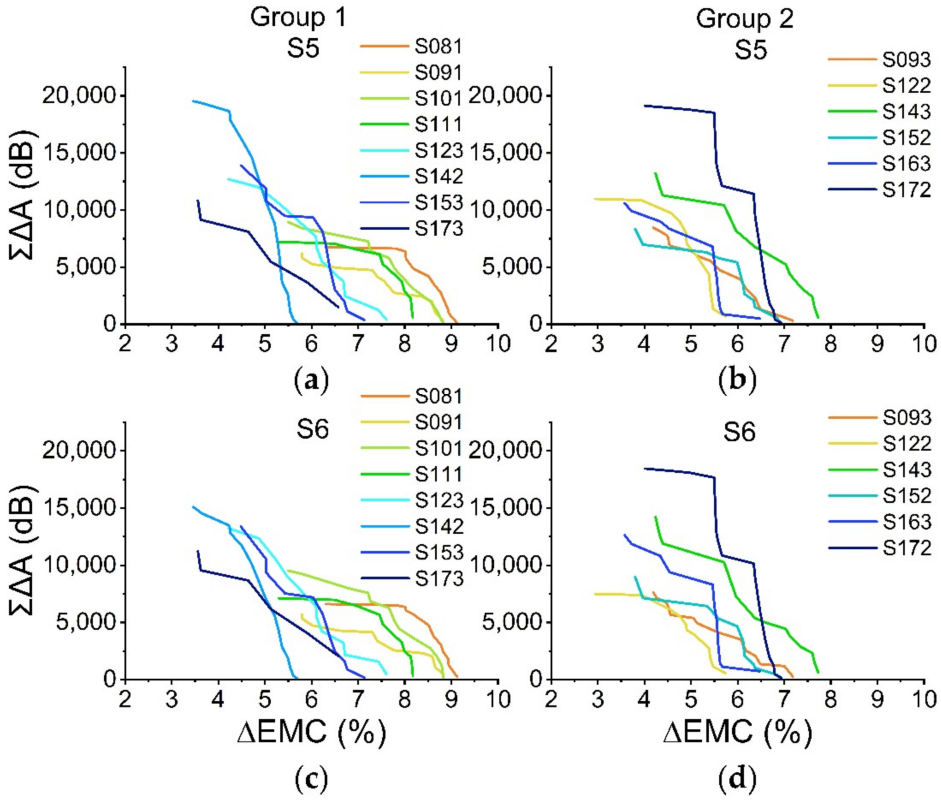

Figure 14. ΣΔA (dB) vs. ΔEMC (%). (**a**) Group 1, S5; (**b**) Group 2, S5; (**c**) Group 1, S6; and (**d**) Group 2, S6.

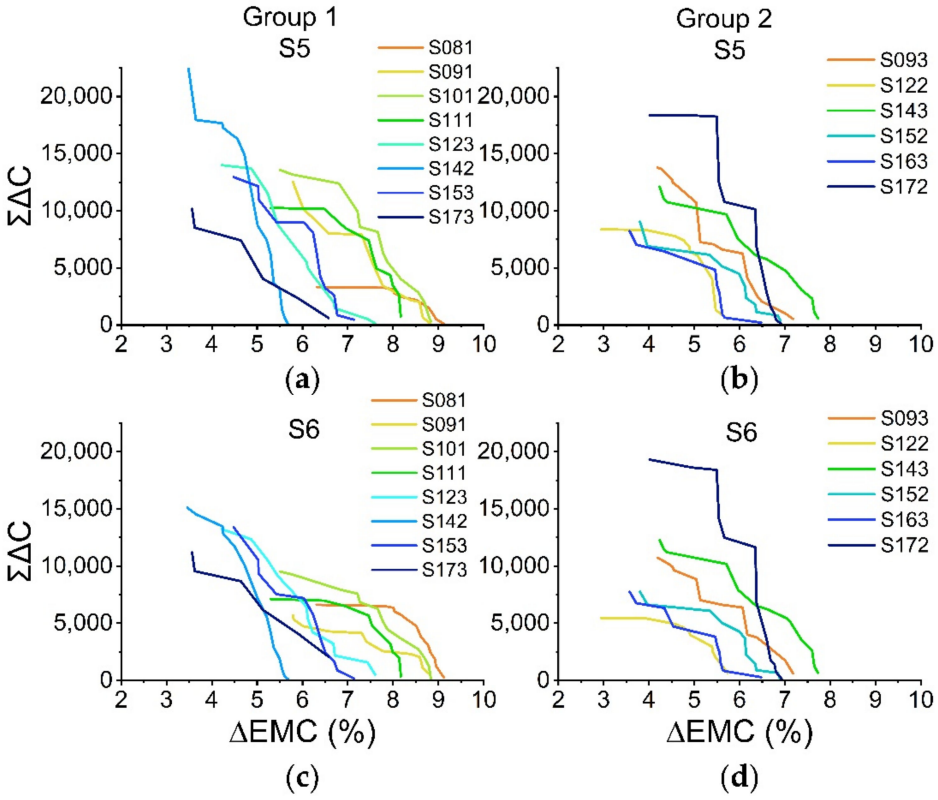

Figure 15. ΣΔC vs. ΔEMC (%). (**a**) Group 1, S5; (**b**) Group 2, S5; (**c**) Group 1, S6; and (**d**) Group 2, S6.

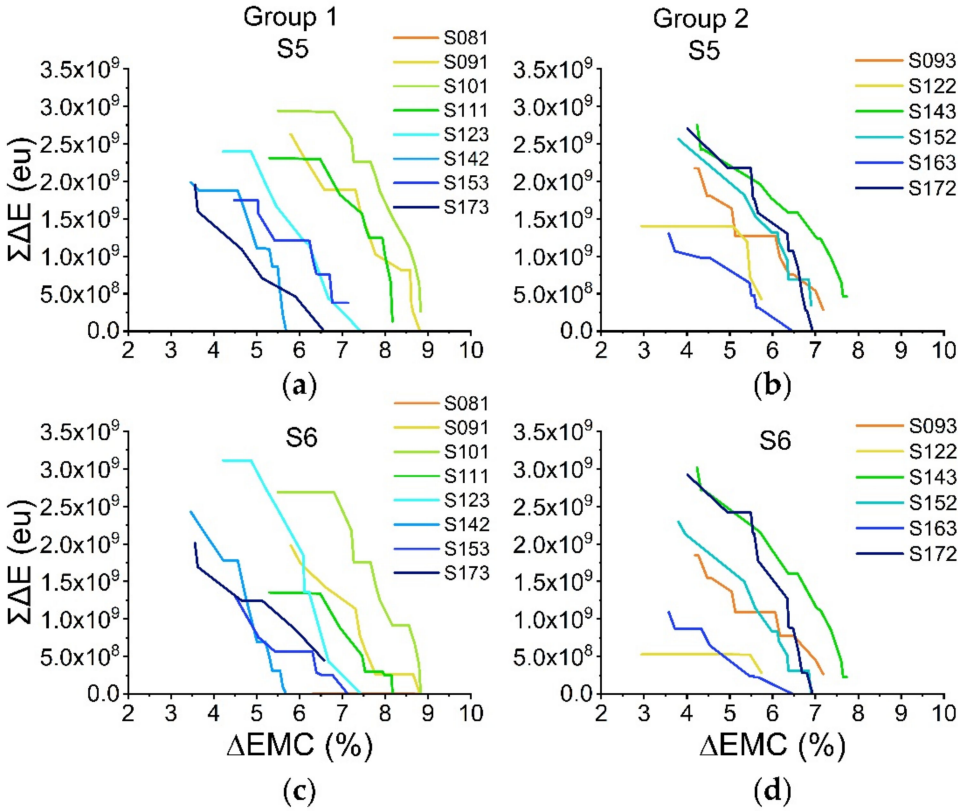

Figure 16. ΣΔE (eu) vs. ΔEMC (%). (**a**) Group 1, S5; (**b**) Group 2, S5; (**c**) Group 1, S6; and (**d**) Group 2, S6. Sample S081 is imperceptible from the graph due to low values of ΣΔE.

Figure 15 reports the cumulative count values (ΣΔC vs. ΔEMC) as line graphs during the whole drying process. The sample analysis shows the same behavior, confirming that the parameters of amplitude and count are influenced in the same way by the EMC in the material. Analyses of dried, natural and saturated specimens reported in the literature [28] showed similar behaviors, with cumulative counts higher in dry samples and smaller in wet samples, confirming the ability to detect acoustic events.

Figure 16 shows ΣΔE vs. ΔEMC. First, sample S081 in Group 1 (for both sensors) showed very low cumulative energy values, almost imperceptible in the graph in the figure, meaning that sample S081 already released the climate-induced stress that may produce AE events. Many samples in both groups (detected by both sensors) showed a plateau, which corresponded to critical points in which energy was not detected. This means that the saturation energy level was reached and no further energy gain occurred because no further drying process happened to samplings, although they were at different equilibrium moisture content concentrations. A plateau can occur for various reasons: for example, due to the presence of any macro or microcrack in the sample that acts as an open joint in reducing the accumulated stress without emitting new AE events, or because the samples were so damaged by climate-induced stresses that they could no longer emit acoustic events when the rest of the sample fractured (e.g., through increase in ductility of the material with increase of other forms of energy different from elastic energy). Thus, each ΣΔE vs. ΔEMC curve in Figure 16 was linearly interpolated in order to calculate the coefficient of energy attenuation (β) according to Equation (7).

Figure 17 shows the coefficient of the attenuation energy rate (β) among the samples. It is worth noticing that, when β is low, the attenuation energy rate (i.e., the energy loss) is at its minimum as the sample is almost dry and, in such a case, the energy detection is optimal; conversely, when β is high, the energy loss is high, as the sample is almost wet. Such a result is in accordance with the effect of moisture content on the propagation of acoustic emission signals in *Pinus massoniana*, as described by Li et al. [15]. Moreover, this

attenuation rate coefficient estimation allows to confirm [8] when the achieved equilibrium moisture content within the sample is homogeneous and low (i.e., when the difference from the initial state is maxima). In such a case, the overall energy of acoustic emission increases, as a consequence of the high strength of dry wood.

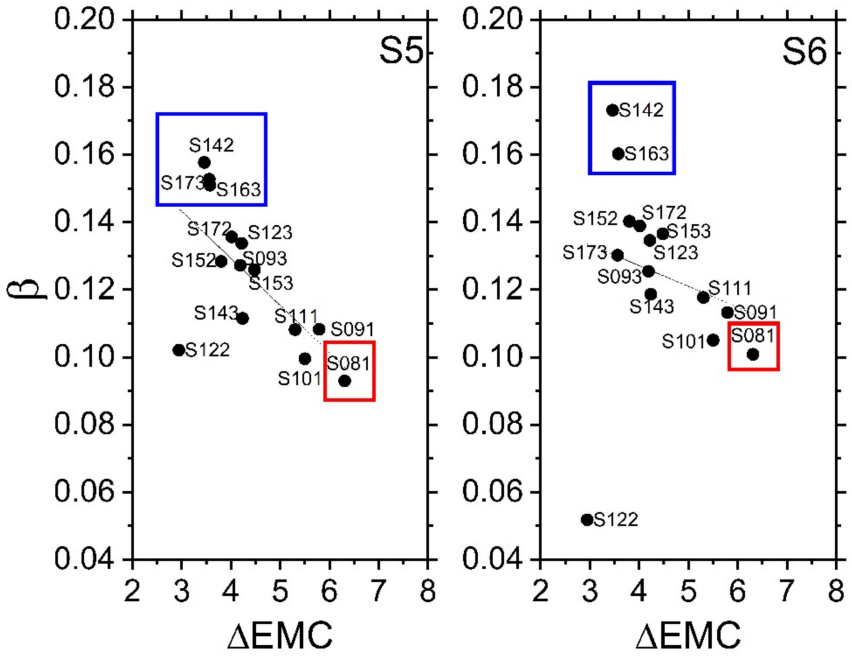

Figure 17. Coefficient of attenuation energy rate (β, in absolute value) per sample along the beam by sensor S5 (**left**) and sensor S6 (**right**). The blue box highlights samples with the lowest moisture gradient during dryness. The red box, shows the opposite, those subjected to the highest moisture gradient.

The samples traced as outliers from the detection of AE parameters (i.e., S081, S142, S172, and S173) demonstrate that an orthotropic and hygroscopic material, such as wood, can have different results depending on the moisture content gradient because of energy attenuation, but also on the internal micro or macroscopic characteristics (presence of knots, open micro cracks, etc.). To differentiate the type of fracture that occurs within the two groups, a punctual visual re-inspection of all the DIC frames was conducted. The categorization of the type of fracture was based on the shape of crack propagation which could depend on the EMC. Group 1 was characterized by samples as having a linear, smooth fracture propagation. On the other hand, Group 2 was characterized as having more pronounced "zig-zag"-like fractures. Higher EMC levels corresponded to more rounded fractures in both groups of specimens. The differences in the fractures are greatly related to the directionality of the carving, which tended to influence the way in which the moisture content gradient behaved within the wooden beam. Moreover, some samples in each group did not fit perfectly into the type of calculation and simulation provided by the adopted formula (Giordano) nor the model. This is the case for S173 (Group 1), with a "zig-zag"-like fracture, and S172 (Group 2), which had a continuous line fracture. Figure 18 shows samples S142 (Group 1) and S172 (Group 2).

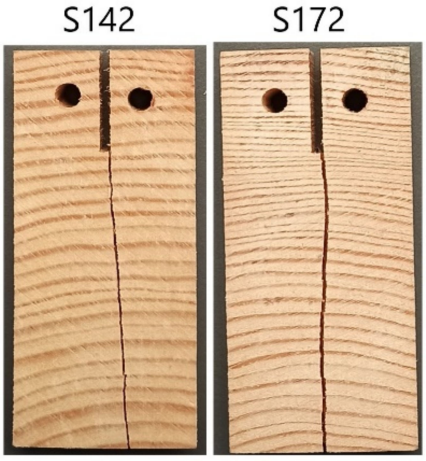

Figure 18. Shape of the fractures in samples S142 (Group 1) and S172 (Group 2).

The acoustic emission non-destructive technique has allowed to detect parameters of amplitude, counts, and energy during the event of brittle fracture in tensile tests. Figures 14–16 show that the parameters of AE change in relation to the equilibrium moisture content. Moreover, after fractography analyses, it is possible to assume that amplitude and counts show similar trends, which are clearly influenced by the level of drying to which a material has been subjected to, resulting in different fracture shapes. The energy had different outcomes and seemed to reproduce the evolution of the EMC of the beam and, also, the existing micro damages, which may also release stress.

4. Conclusions

The procedure developed in this research proved to be effective to calibrate acoustic emission parameters (amplitude, counts, and energy) with respect to the equilibrium moisture content of Scots pine. Indeed, amplitude and counts can be used as proxies for perceptibility of fracture events in relation to the equilibrium moisture content gradient experienced by the samples after a natural drying process. If the dryness is almost complete, amplitude and counts easily detect the acoustic emissions released by brittle events and vice versa. Energy can be used to derive the coefficient of energy attenuation rate that allows to directly relate the energy loss (gain) with the low (high) equilibrium moisture content gradient experienced by the samples after a natural drying process.

In addition, this research has proven that acoustic emissions allow to:

- identify pre-existing macro or micro cracks in samples, which act as an open joint, reducing accumulated stress without emitting new acoustic emission events.
- point out damage caused by moisture variations, i.e., when the increasing ductility of the material generates no elastic energy.

This opens interesting perspectives for the use of the acoustic emission technique as a preventive conservation tool, as it allows to record events related to natural drying processes or the presence of internal defects.

The fields of application are multiple: architecture, engineering studies, cultural heritage, and more. In fact, acoustic emissions can be interpreted as a new way of understanding the state of conservation of a hygroscopic material and can be used for in situ monitoring. Moreover, through an in-depth study, the analysis proposed in this work can yield feedback on any wooden material, starting from the smallest artifacts to historic and non-historic buildings, which can be evaluated using the acoustic emission non-destructive technique.

Author Contributions: B.B.: interpretation of data and analyses, data discussion and writing—original draft preparation, conceptualization. F.F.: data discussion, conceptualization, supervision, review and editing writing. A.M.S.: data discussion, conceptualization, supervision, review and edit-

ing and writing. C.B.: conceptualization, funding acquisition, methodology, project administration, resources, supervision, review and editing and writing. All authors have read and agreed to the published version of the manuscript.

Funding: This research was funded by the Norwegian Research Council through the SyMBoL Project (project no. 274749). B.B is indebted to the Erasmus+ Traineeship exchange program.

Acknowledgments: C.B. is indebted to the technical staff of the Mechanical and Industrial Engineering (MTP) department of NTNU and the NTNU wood center. Special thanks to Carl-Magnus Mitbø, Børge Holen, and Lavinia de Ferri, which Post Doc position was financed by SyMBoL, which contributed to perform the calibration tests conceived by C.B. as principal investigator and coordinator of the SyMBoL Project. C.B. and A.M.S. acknowledge the support of the Norwegian Research Council through the SyMBoL Project (project no. 274749) and of the Erasmus+ Traineeship exchange program.

Conflicts of Interest: The authors declare no conflict of interest.

Appendix A

This section reports the Equations (A1)–(A7) regarding the multiple regressions tested. Furthermore, Figure A1 shows the eight models in scatter-plots graphs and Tables A2 and A1 provides the statistical parameters and the coefficients related to all the equations tested.

$$y = b_0 + b_1x_1 + b_2x_2 + b_3x_1x_2 \quad \text{(A1)}$$

$$y = b_0 + b_1x_1 + b_2x_2 + b_3x_1^2 \quad \text{(A2)}$$

$$y = b_0 + b_1x_1 + b_2x_2 + b_3x_1x_2 + b_4x_1^2 \quad \text{(A3)}$$

$$y = b_0 + b_1x_1 + b_2x_2 + b_3x_1x_2 + b_4x_1^2 + b_5x_2^2 \quad \text{(A4)}$$

$$y = b_0 + b_1x_1 + b_2x_2 + b_3x_1x_2 + b_4x_1^2 + b_5x_2^2 + b_6x_1^2x_2^2 \quad \text{(A5)}$$

$$y = b_0 + b_1x_1 + b_2x_2 + b_3x_1x_2 + b_4x_1^2x_2^2 \quad \text{(A6)}$$

$$y = b_0 + b_1x_1 + b_2x_2 + b_3x_1x_2 + b_4x_1^2 + b_5x_2^2 + b_6\sqrt{x_1^2 + x_2^2} \quad \text{(A7)}$$

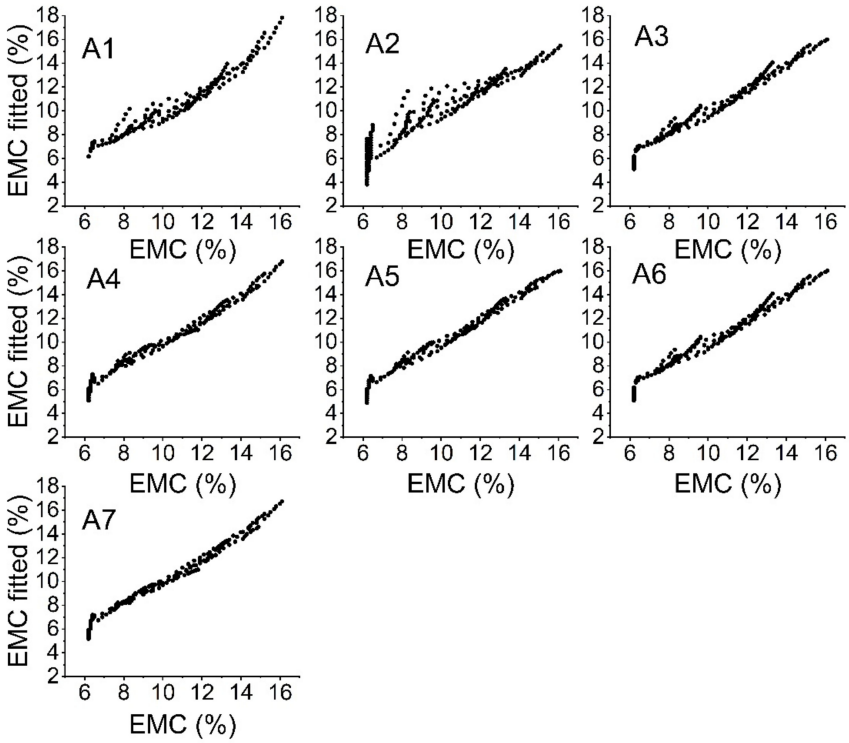

Figure A1. Seven multiple regressions tried for the equilibrium moisture content analysis.

Table A1. Statistical parameters associated to the equations tested. Adjusted coefficient of determination $\overline{R}^2$, the standard error E_{STD}, and the number of the equation associated to each regression.

Equation	$\overline{R}^2$	E_{STD}
(A1)	0.96	0.59
(A2)	0.89	0.93
(A3)	0.98	0.42
(A4)	0.98	0.42
(A5)	0.98	0.37
(A6)	0.98	0.42
(A7)	0.98	0.38

Table A2. Intercepts and coefficients associated to x_1 and x_2 (radial and longitudinal directions) for each model of regression indicated with the number of equation (Equation).

Equation	Coefficients (b)							
	Int.	x_1	x_2	$x_1 \cdot x_2$	${x_1}^2$	${x_2}^2$	${x_1}^2 \cdot {x_2}^2$	$\sqrt{x_1^2+x_2^2}$
(A1)	6.06	1.33×10^{-2}	-2.48×10^{-3}	2.38×10^{-4}				
(A2)	1.19	1.27×10^{-1}	1.06×10^{-2}		-3.65×10^{-4}			
(A3)	6.79	-2.35×10^{-2}	-7.89×10^{-3}	5.09×10^{-4}	-3.97×10^{-9}			
(A4)	2.64	5.34×10^{-2}	1.68×10^{-2}	2.38×10^{-4}	-3.65×10^{-4}	-3.11×10^{-5}		
(A5)	4.94	-1.16×10^{-2}	5.28×10^{-3}	4.48×10^{-4}	-3.27×10^{-5}	-1.93×10^{-5}	-3.07×10^{-9}	
(A6)	6.79	-2.35×10^{-2}	-7.89×10^{-3}	5.09×10^{-4}			-3.97×10^{-9}	
(A7)	3.15	9.41×10^{-2}	1.98×10^{-1}	1.14×10^{-4}	-4.60×10^{-5}	-1.61×10^{-5}		-1.88×10^{-1}

References

1. Cagnana, A.I.L. *Archeologia dei Materiali da Costruzione*; S.A.P. Società Archeologica s.r.l.: Mantova, Italy, 2000; pp. 215–231.
2. Berti, S. *Le Biomasse Legnose: Il Legno*; Volume Biomasse Forestali ad Uso Energetico in Ambiente Alpino: Potenzialità e Limiti; Consiglio Nazionale delle Ricerche (CNR): Rome, Italy, 4 June 2007.
3. SyMBoL–Sustainable Management of Heritage Buildings in a Long-Term Perspective-NTNU. Available online: https://www.ntnu.edu/symbol (accessed on 9 April 2021).
4. Dario, C.; Limpens-Neilen, D.; Shellen, H.L. *Roman, Kozlowsky Church Heating and the Preservation of the Cultural Heritage Guide to the Analysis of the Pros and Cons of Various Heating Systems*; Electa: Milan, Italy, 2007; ISBN 88-370-5034-8.
5. Bartolucci, B.; De rosa, A.; Bertolin, C.; Berto, F.; Penta, F.; Siani, A.M. Mechanical Properties of the Most Common European Woods: A Literature Review. *Frat. Ed Integrità Strutt.* **2020**, *54*, 249–274. [CrossRef]
6. Li, Z.; Jiang, J.; Lyu, J.; Cao, J. Orthotropic Viscoelastic Properties of Chinese Fir Wood Saturated with Water in Frozen and Non-Frozen States. *For. Prod. J.* **2021**, *71*, 77–83. [CrossRef]
7. Li, X.; Li, M.; Ju, S. Frequency Domain Identification of Acoustic Emission Events of Wood Fracture and Variable Moisture Content. *For. Prod. J.* **2020**, *70*, 107–114. [CrossRef]
8. Jakieła, S.; Bratasz, Ł.; Kozłowski, R. Acoustic Emission for Tracing Fracture Intensity in Lime Wood Due to Climatic Variations. *Wood Sci. Technol.* **2008**, *42*, 269–279. [CrossRef]
9. Jakiela, S.; Bratasz, L.; Kozlowski, R. Acoustic Emission for Tracing the Evolution of Damage in Wooden Objects. *Stud. Conserv.* **2007**, *52*, 101–109. [CrossRef]
10. Łukomski, M.; Strojecki, M.; Pretzel, B.; Blades, N.; Beltran, V.; Freeman, A. Acoustic Emission Monitoring of Micro-Damage in Wooden Art Objects to Assess Climate Management Strategies. *Insight Non Destr. Test. Cond. Monit.* **2017**, *59*, 256–264. [CrossRef]
11. Perrin, M.; Yahyaoui, I.; Gong, X. Acoustic Monitoring of Timber Structures: Influence of Wood Species under Bending Loading. *Constr. Build. Mater.* **2019**, *208*, 125–134. [CrossRef]
12. Barbosh, M.; Sadhu, A.; Sankar, G. Time–Frequency Decomposition-Assisted Improved Localization of Proximity of Damage Using Acoustic Sensors. *Smart Mater. Struct.* **2021**, *30*, 025021. [CrossRef]
13. El-Hadad, A.; Brodie, G.I.; Ahmed, B.S. The Effect of Wood Condition on Sound Wave Propagation. *Open J. Acoust.* **2018**, *8*, 37. [CrossRef]
14. Yang, L.; FeiYun, X. Acoustic emission signal characteristics of Pinus yunnanensis with different moisture content. *Sci. Silvae Sin.* **2019**, *55*, 96–102.
15. Li, X.; Ju, S.; Luo, T.; Li, M. Effect of Moisture Content on Propagation Characteristics of Acoustic Emission Signal of Pinus Massoniana Lamb. *Eur. J. Wood Wood Prod.* **2020**, *78*, 185–191. [CrossRef]
16. Bertolin, C.; De Ferri, L.; Berto, F. Calibration Method for Monitoring Hygro-Mechanical Reactions of Pine and Oak Wood by Acoustic Emission Nondestructive Testing. *Materials* **2020**, *13*, 3755. [CrossRef] [PubMed]

17. Aicher, S.; Höfflin, L.; Dill-Langer, G. Damage Evolution and Acoustic Emission of Wood at Tension Perpendicular to Fiber. *Holz Als Roh Werkst.* **2001**, *59*, 104–116. [CrossRef]
18. MTS Criterion® Series 40 Electromechanical Universal Test Systems. Available online: https://test.mts.com/-/media/materials/pdfs/brochures/100-262-929d_criterionem40.pdf?as=1 (accessed on 9 April 2021).
19. Stingray. The Transformer Camera. Available online: https://www.1stvision.com/cameras/AVT/dataman/Stingray_DataSheet_F504BC_fiber_V1.1.1.pdf (accessed on 9 April 2021).
20. AMSY-6 System Description. Available online: https://www.vallen.de/zdownload/pdf/AMSY-6_Description.pdf (accessed on 9 April 2021).
21. Baensch, F. Damage Evolution in Wood and Layered Wood Composites Monitored in Situ by Acoustic Emission, Digital Image Correlation and Synchrotron Based Tomographic Microscopy. Ph.D. Thesis, ETH Zurich, Zurich, Switzerland, 2015.
22. Kretschmann, D.E. Mechanical Properties of Wood. In *Wood Handbook, Wood as an Engineering Material*; Forest Products Laboratory: Madison, WI, USA, 2010; pp. 1–44.
23. Tresenteret. Available online: http://www.tresenter.no/aktuelt/ntnu-og-tresenteret-etablerer-nytt-senter-ntnu-wood (accessed on 9 April 2021).
24. Camuffo, D. Thermodynamics for Cultural Heritage. In *Physics Methods in Archaeometry*; Martini, M., Milazzo, M., Piacentini, M., Eds.; IOS Press: Varenna, Italy; Amsterdam, The Netherlands, 2004; pp. 37–98.
25. Marco, M. *Climate Risk Assessment in Museums: Degradation Risks Determined from Temperature and Relative Humidity Data*; Technische Universiteit Eindhoven: Eindhoven, The Netherlands, 2012.
26. Giordano, G. *Tecnologia Del Legno. La Materia Prima*; UTET: Torino, Italy, 1981; Volume 1.
27. Camuffo, D. *Microclimate for Cultural Heritage-Measurments, Risk Assessment, Conservation, Restoration, and Maintenance of Indoor and Outdoor Monuments*, 3rd ed.; Elsevier: Amsterdam, The Netherlands, 2019.
28. Li, S.; Wu, G.; Shi, H. Acoustic Emission Characteristics of Semi-Rigid Bases with Three Moisture Conditions during Bending Tests. *Road Mater. Pavement Des.* **2017**, *20*, 187–198. [CrossRef]